of blowing RNLN. These images show that the vortices are reasonably symmetrical and well defined. Even when the wing is near the maximum roll amplitude, the vortices are almost symmetrical and level, as shown in image b). This set of control rule base was found to decrease the amplitude of wing rock.

The force balance experiment is conducted to establish the change in total pitching moment. The results are summarized in Fig. 8. The results indicated that the onset of wing rock causes a substantial decrease in the total pitching moment. Three sets of rule base are tested. They indicated that blowing LRRL further decreases the total pitching moment, whereas blowing RLLR and RNLN increases the total pitching moment. Generally, pitching moment is reduced when the amplitude of the rocking motion is amplified, and pitching moment is increased as the wing rock motion is weakened. Blowing LRRL increases the instability of the wing rock, whereas blowing RLLR or RNLN decreases its instability.

Figure 9 illustrates the roll response of blowing LRRL. The steady amplitude of wing rock reaches a higher value. The control input of blowing LRRL has aggravated the wing rock conditions and has resulted in an overall amplitude increase of about 25%.

Figure 10 illustrates the roll response of blowing RNLN. Figure 10a shows that the amplitude of wing rock is decaying over the time span of 10 s. Figure 10b shows the amplitude of the wing rock before suppression and after it is fully suppressed. The solid line indicates the amplitude of the wing rock after it is fully suppressed. This clearly demonstrates that the chosen rule base of RNLN with recessed angle blowing is very effective in suppressing the wing rock.

## Conclusions

The roll response obtained shows that the wing rock amplitude increases as the control input of blowing LRRL is applied. Because this set of control input generates reaction force on the wing that opposes the wing rock motion, the increase in the wing rock amplitude must be caused by the adverse change in the vortices from the effects of blowing LRRL.

Conversely, the wing rock amplitude decays as the control input of blowing RNLN is applied. This set of control input generates reaction force on the wing that assists the wing rock motion. The decrease in the wing rock amplitude must be caused by the desired change in the vortices from the effects of blowing RNLN. The blowing coefficient is approximately estimated to be 0.033. The strength and positions of the vortices are affected by the blowing technique. The application of the RASB technique is to achieve a neutralization of the vortex asymmetry that occurs during wing rock. Arena and Nelson[7] stated that the hysteresis behavior in the normal position of the vortices is the prime candidate for the mechanism responsible for wing rock. During the wing rock motion, one vortex stays attached close to the wing surface while the other vortex goes through the vortex liftoff process to supply the wing rock mechanism. Flow visualization using the digital camera indicated that blowing causes the vortices to lift off from the wing surface. This observed change in the normal position of the vortex as a result of blowing is therefore an important criterion that might be responsible for the suppression of wing rock.

The effectiveness of the RASB technique lies in its ability to enlarge the associated vortex subjected to blowing and also to lift the vortex off the surface of the wing without causing vortex breakdown. Total lift over the wing is reduced on the onset of wing rock. The enlargement of the vortex subjected to blowing created the additional lift to restore the total lift to its original level. Vortex liftoff created the asymmetry necessary to initiate wing rock. The liftoff process of the vortex subjected to blowing counteracts this asymmetry to restore stability.

## Acknowledgments

Authors would like to express thanks to Rik Heslehurst, Senior Lecturer, Australian Defence Force Academy, University of New South Wales for his suggestions in improving the presentation of the paper. We would like to place on record our appreciation for the reviewers for their suggestions for improving the presentation of the paper.

## References

[1] Nayfeh, A. H., Elzebda, J. M., and Mook, D. T., "Development of an Analytical Model of Wing Rock for Slender Delta Wings," *Journal of Aircraft*, Vol. 26, No. 8, 1989, pp. 737–743.

[2] Ng, T. T., Suarez, C. J., and Malcom, G. N., "Forebody Vortex Control for Wing Rock Suppression," *Journal of Aircraft*, Vol. 31, No. 2, 1994, pp. 298–305.

[3] Johari, H., Olinger, D. J., and Fitzpatrick, K. C., "Delta Wing Vortex Control via Recessed Angled Spanwise Blowing," *Journal of Aircraft*, Vol. 32, No. 4, 1995, pp. 804–810.

[4] Johari, H., and Moreira, J., "Delta Wing Vortex Manipulation Using Pulsed and Steady Blowing During Ramp-Pitching," *Journal of Aircraft*, Vol. 33, No. 2, 1994, pp. 304–310.

[5] Arena, A. S., Nelson, R. C., and Schiff, L. B., "The Effect of Asymmetric Vortex Wake Characteristics on a Slender Delta Wing Undergoing Wing Rock Motion," AIAA Paper 89-3348, Aug. 1989.

[6] Arena, A. S., Nelson, R. C., and Schiff, L. B., "An Experimental Study of the Non-Linear Dynamic Phenomenon Known as Wing Rock," AIAA Paper 90-2812, Aug. 1990.

[7] Arena, A. S., and Nelson, R. C., "Experimental Investigation on Limit Cycle Wing Rock of Slender Wings," *Journal of Aircraft*, Vol. 31, No. 5, 1994, pp. 1148–1155.

# Computational Investigation of Flow Through a Louvered Inlet Configuration

Ismail H. Tuncer*
*Middle East Technical University, 06531 Ankara, Turkey*
and
Max F. Platzer†
*Naval Postgraduate School, Monterey, California 93943*

## Introduction

THE aerodynamic analysis of subsonic lifting body concepts for future unmanned air vehicles and missiles has been an active research field in recent years. A lifting body, as shown in Fig. 1, combines three emerging technologies, namely, lifting body, thrust vector control, and flush louvered inlet. The flush louvered inlet configuration requires the flow to turn 360 deg in the plenum chamber before entering the engine. The pressure losses and flow distortions experienced in the plenum chamber are serious concerns. In the analysis of the flow, the boundary-layer buildup on the underside of the missile body before reaching the louvered inlet and the three-dimensional flow in the plenum chamber are to be accounted for. Engine tests simulating flows through such an inlet configuration are currently not possible. It is, therefore, highly desirable to compute viscous, compressible flows through a typical flush louvered inlet configuration.

In this work, a numerical study of viscous, subsonic flow through a louvered inlet configuration is performed. In the design of louvered inlets, inlet vanes are required to achieve good total pressure recovery. However, in this analysis, the inlet vanes are not modeled

Presented as Paper 01-2477 at the AIAA 19th Applied Aerodynamics Conference, Anaheim, CA, 11–14 June 2001; received 31 January 2002; revision received 6 May 2002; accepted for publication 14 May 2002. 

*Associate Professor, Department of Aerospace Engineering; tuncer@ae.metu.edu.tr. Member AIAA.

†Distinguished Professor, Department of Aero/Astronautics; platzer@aa.nps.navy.mil. Fellow AIAA.

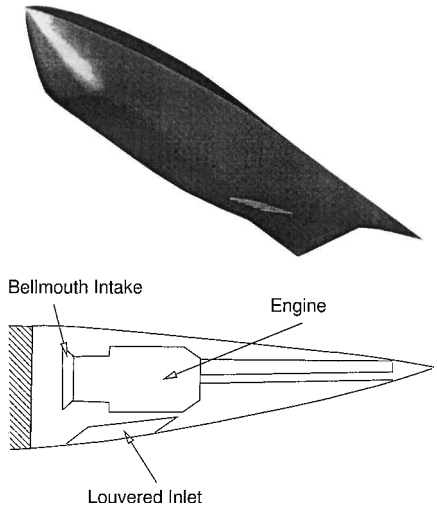


**Fig. 1 Typical subsonic lifting body and a louvered inlet configuration.**

to simplify the computational domain. Preliminary flow solutions of this highly complex flowfield are first obtained, and the variation of the mass flow rate and the total pressure recovery at the engine intake is evaluated as a function of the imposed intake pressure.

The Navier–Stokes solver, OVERFLOW (ver. 1.7v), is used to compute the flow through the louvered inlet configuration. OVERFLOW, which was developed at NASA Ames Research Center, is a compressible, thin-layer, Reynolds averaged Navier–Stokes solver.[1] It accommodates computational domains discretized with overset subgrids. Overset subgrids are preprocessed with the PEGSUS code, which determines the intergrid boundaries created by the overset subgrids. At the intergrid boundaries, OVERFLOW interpolates the flow variables from the neighboring donor subgrids. PEGSUS provides the intergrid interpolation stencils and the corresponding interpolation weights to OVERFLOW. In the past, we have successfully computed viscous flowfields over missile configurations using OVERFLOW.[2,3]

## Computational Domain

The flowfield is assumed to be symmetric with respect to the midplane of the inlet configuration, and only half of the flow domain is discretized. The flow domain consists of four distinct regions, the external flow region underside of the missile body, the inlet passage, the plenum chamber, and the engine intake. The plenum chamber is about 0.4 m long, 0.4 m wide and 0.6 m deep. Because inlet vanes are not modeled in this preliminary study, the inlet is discretized as a rectangular opening.

The computational domain is discretized using overset grids (Fig. 2). The overset grid system consists of four subgrids: Grids for the external flow region ($66 \times 31 \times 51$), the inlet passage ($59 \times 41 \times 33$), the plenum chamber ($81 \times 71 \times 91$), and the engine intake with a bellmouth ($99 \times 41 \times 41$). The total number of grid points is about $9 \times 10^5$. To resolve the boundary-layer flows at the wall boundaries, the first grid spacing on the wall boundaries varies from $2.5 \times 10^{-5}$ m on the outer wall to $2 \times 10^{-4}$ m on the plenum chamber and the bellmouth intake walls. The subgrid for the inlet passage is overset onto the neighboring subgrids in the plenum chamber and the external flow regions. In the middle part of its outer boundaries that covers the wall boundaries of the inlet passage, the wall boundary conditions are imposed. In the remaining part of its outer boundaries that oversets onto the neighboring subgrids, the intergrid boundary conditions are successfully applied.

## Numerical Results

The OVERFLOW solver has several discretization and time-integration schemes available. In this study, the three-factor diagonal scheme with central differenced convective flux terms, which is the fastest and the most robust, is used. The central difference smoothing coefficient is gradually reduced to 0.10 from the starting value of 0.25. Local time stepping is used to obtain the steady-state solution. A constant pressure based on the $P_{\text{intake}}/P_\infty$ ratio is applied at the engine intake surface.

**Table 1 Influence of intake pressure on the intake flow[a]**

| $P_{\text{intake}}/P_\infty$ | $\dot{m}$, kg/s | $\bar{P}_{0_{\text{intake}}}/\bar{P}_{0_\infty}$ | $\bar{M}_{\text{intake}}$ |
|---|---|---|---|
| 0.80 | 5.95 | 0.60 | 0.437 |
| 0.60 | 7.88 | 0.57 | 0.74 |
| 0.50 | 8.30 | 0.56 | 0.90 |

[a] $M_\infty = 0.8$, $T_\infty = 260$ K, and $Re = 1.5 \times 10^8$.

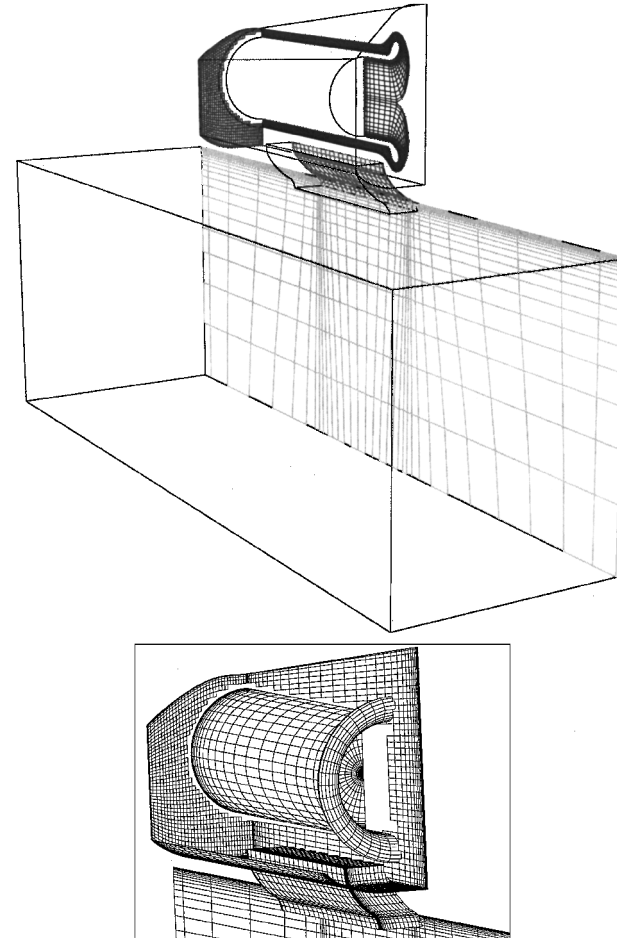

**Fig. 2 Computational domain discretized with overset grids (every other grid point is plotted).**

Flows through the flush-louvered inlet were computed at three different engine intake pressure ratios using the Baldwin–Lomax and the Baldwin–Barth turbulence models. All of the computations were carried out on a Cray-J916/4. A typical converged solution took about 6000 time steps in approximately 60 CPU h. All of the viscous flowfields were computed at $M_\infty = 0.8$, $T_\infty = 260$ K, and $Re = 1.5 \times 10^8$/m assuming a fully turbulent flow. The computed flow conditions and the results are summarized in Table 1, where $\dot{m}$ is the mass flow rate through the engine intake, $\bar{P}_{0\text{intake}}/P_{0_\infty}$ is the area averaged total pressure recovery ratio, and $\bar{M}_{\text{intake}}$ is the area averaged Mach number at the engine intake boundary.

The Baldwin–Lomax algebraic turbulence model was first employed. However, the computations suffered from slow convergence and instabilities in the flow.[4] The unacceptable performance of the model is attributed to the low eddy-viscosity values the model predicts near the side walls of the plenum chamber. Note that the Baldwin–Lomax model computes the normal distance to the wall

boundaries separately for each wall surface and, therefore, is expected to fail at the corner regions of closed domains like the plenum chamber. On the other hand, the Baldwin–Barth turbulence model computes the eddy viscosities based on the closest distance from any wall and was found to be well behaved in the computation of the fully turbulent flow in the plenum chamber.

The flow computed at $P_{\text{intake}}/P_{\infty} = 0.80$ with the Baldwin–Barth model is shown in Figs. 3–6. The velocity vectors (Fig. 3) and

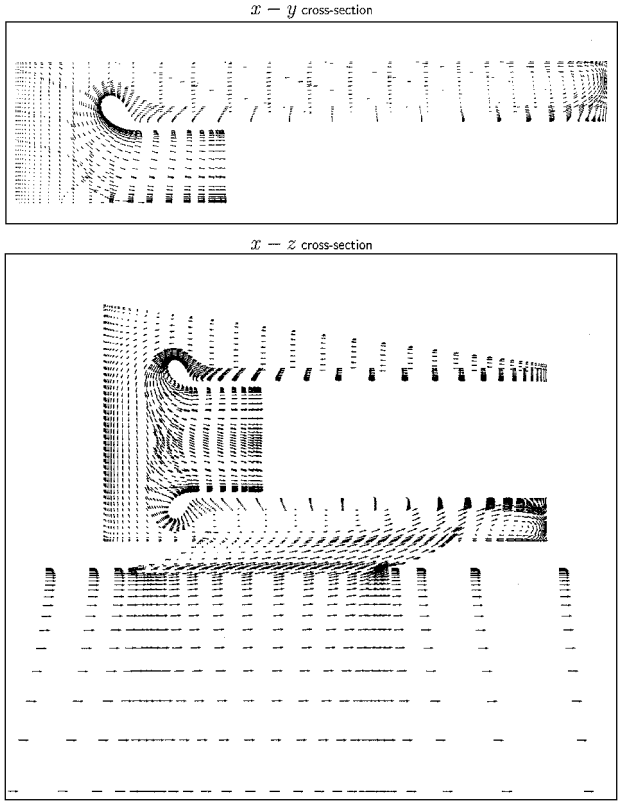


**Fig. 3 Velocity field computed at $P_{\text{intake}}/P_{\infty} = 0.80$.**

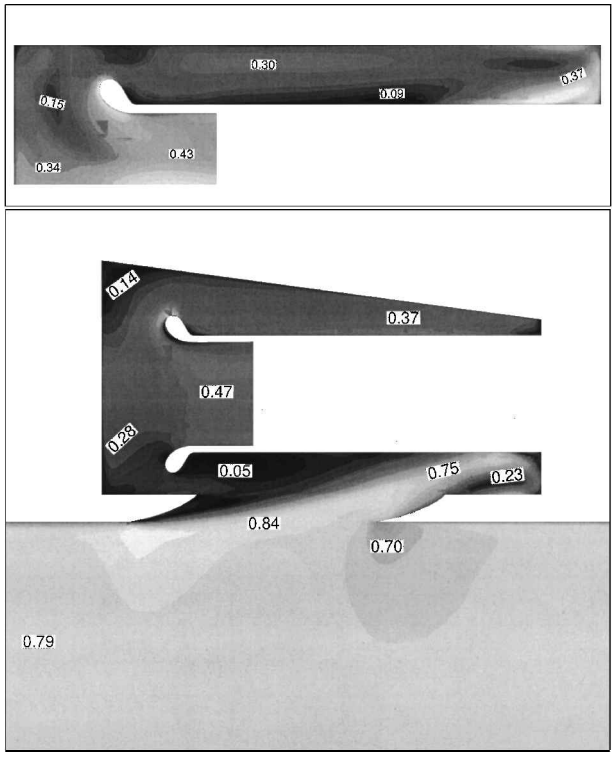


**Fig. 4 Mach number distribution computed at $P_{\text{intake}}/P_{\infty} = 0.80$.**

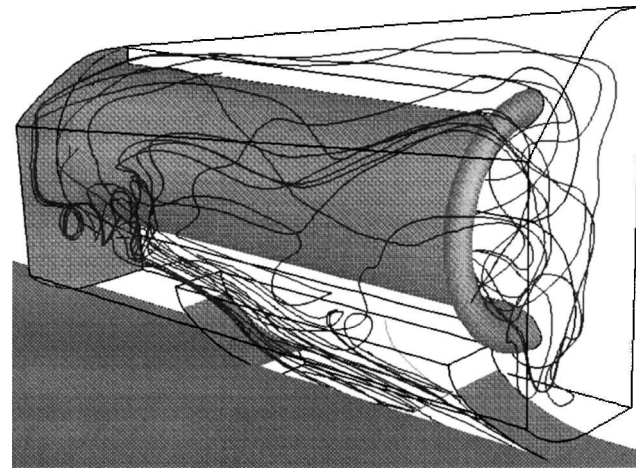

**Fig. 5 Particle traces computed at $P_{\text{intake}}/P_{\infty} = 0.80$.**

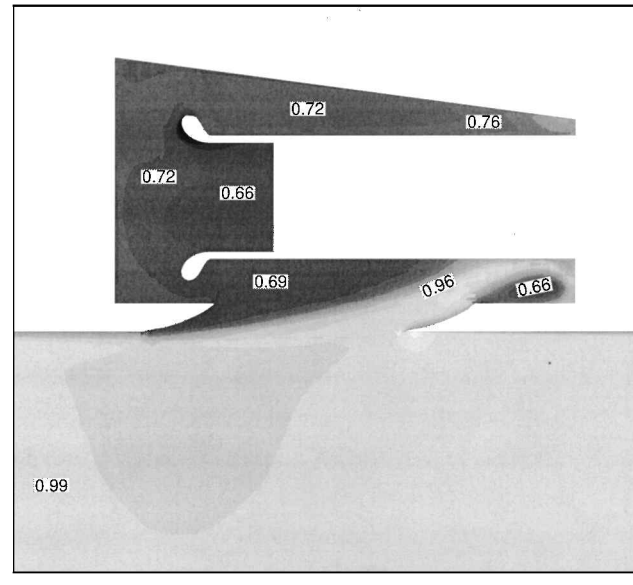


**Fig. 6 Total pressure recovery distribution at $P_{\text{intake}}/P_{\infty} = 0.80$.**

the Mach number distribution (Fig. 4) at the cross-sectional planes through the engine intake, as well as the particle traces (Fig. 5) through the inlet, reveal the highly complex nature of the flow in the plenum chamber. As the incoming flow hits the back end of the plenum chamber, vortical structures and recirculating flows are formed. However, a significant percentage of the flowfield in the chamber is covered with low-velocity, dead flow zones. The flow that results in an average 60% total pressure recovery at the engine (Fig. 6) intake produces a mass flow rate of 5.95 kg/s. The flows computed at higher reduced pressure ratios at the engine intake, $P_{\text{intake}}/P_{\infty}$, produce higher mass flow rates at slightly increased total pressure losses as given in Table 1. Yet the intake Mach number increases significantly, and supersonic velocities are observed in the flow.

## Conclusions

The preliminary flow solutions show that the flow distortion in the plenum chamber and the pressure losses are significant, yet a sufficient amount of mass flow rate may be achieved at the expense of total pressure recovery. The results suggest that the inlet vanes and an optimization of the inlet configuration are needed to alleviate the pressure losses and to increase the efficiency of a louvered inlet.

## Acknowledgment

This investigation was supported by the Naval Air Warfare Center, China Lake, California.

## References

[1]Buning, P., Jespersen, D. C., Pulliam, T. H., Chan, W. M., Slotnick, J. P., Krist, S. E., and Renze, K. J., *OVERFLOW User's Manual*, Ver. 1.7v, NASA Ames Research Center, Moffet AFB, CA, 1995.

[2]Tuncer, I. H., and Platzer, M. F., "Computational Study of Subsonic Flow over a Close-Coupled Delta Canard-Wing-Body Configuration," *Journal of Aircraft*, Vol. 35, No. 4, 1998, pp. 554–560.

[3]Tuncer, I. H., Platzer, M. F., and VanDyken, R. D., "Navier–Stokes Analysis of Subsonic Flowfields over a Missile Configuration," *Journal of Spacecraft and Rockets*, Vol. 35, No. 2, 1998, pp. 127–131.

[4]Tuncer, I. H., and Platzer, M. F., "Computational Investigation of Flow Through a Louvered Inlet Configuration," AIAA Paper 01–2477, June 2001.


# Angle-of-Attack Effect on Transonic/ Supersonic Aeroelasticity of Wing-Box Model


Jae-Han Yoo,* Dong-Hyun Kim,† and In Lee‡
*Korea Advanced Institute of Science and Technology, Taejon 305-701, Republic of Korea*


## Introduction

AN understanding of the aeroelastic behavior of flight vehicles in the transonic and low-supersonic regimes is of great importance for flight safety. The flutter boundary in this regime varies with changes in the initial angle of attack. Aeroelastic analyses and experiments on the effect of initial angle of attack have been performed previously. Early studies of the two-degree-of freedom airfoil system were performed using the HYTRAN2 (Ref. 1) and an Euler code.[2] For a three-dimensional wing at high angles of attack in incompressible flow, there is the work by Strganac and Mook.[3] In their paper, using the unsteady vortex-lattice method, the equations of motion were integrated, considering the nonlinear effects of the separated vortex. Yates et al.[4] analyzed the effect of angle of attack on a large aspect ratio transport-type wing with a supercritical airfoil, using a modified strip analysis employing wind-tunnel steady aerodynamic data. Also, the CAP-TSD code[5] has been applied to the active flexible wing wind-tunnel model to investigate static and dynamic aeroelastic behaviors below Mach 0.95. These studies provide a good foundation for understanding initial angle-of-attack effects, both theoretically and practically, and motivated by this, we will examine in detail the effect of both positive and negative angles of attack on a typical fighter wing-box model with an asymmetric airfoil in the transonic and low-supersonic flow regions. The critical effect of a negative angle of attack and unusual frequency changes due to the effect of normal shocks are presented. The computed steady aerodynamic results for rigid and deformed shapes of the model are presented and compared. Also, detailed dynamic aeroelastic responses are computed using a coupled time-marching method based on the effective computational structural dynamic (CSD) and computational fluid dynamic (CFD) techniques,[6] which are similar to those used in Ref. 5. CSD analyses for the wing-box model have been performed using MSC/NASTRAN. The variations of flutter boundary due to the change of initial angles of attack are also compared for several Mach numbers.

Received 10 December 2001; revision received 20 May 2002; accepted for publication 20 May 2002. 


*Graduate Research Assistant, Department of Aerospace Engineering, 373-1 Kusong-dong, Yusong-gu.

†Postdoctoral Research Associate, Department of Aerospace Engineering, 373-1 Kusong-dong, Yusong-gu. Member AIAA.

‡Professor, Department of Aerospace Engineering, 373-1 Kusong-dong, Yusong-gu. Senior Member AIAA.


## Computational Method

The aeroelastic equations of motion for an elastic wing can be formulated in terms of generalized displacement response vector $\{q(t)\}$, which is a solution of the following equation:

$$[M_g]\{\ddot{q}(t)\} + [C_g]\{\dot{q}(t)\} + [K_g]\{q(t)\} = \{Q(t, q, \dot{q})\} \quad (1)$$

where $[M_g]$ is the generalized mass matrix, $[C_g]$ is the generalized damping matrix, and $[K_g]$ is the generalized stiffness matrix. $\{Q\}$ is the vector of generalized aerodynamic forces computed by integrating the pressure distributions on the wing surface as

$$Q(t)_i = \frac{1}{2}\rho U^2 c_r^2 \iint_S \left[C_{p_L}(x, y, t) - C_{p_U}(x, y, t)\right]\psi_i(x, y)\frac{\mathrm{d}S}{c_r^2} \quad (2)$$

where $\rho$ is the freestream air density; $U$ is the freestream velocity; $c_r$ is the reference chord length; $S$ is the wing area; $C_p$ is the unsteady pressure coefficient on the arbitrary wing surface; the subscripts $L$ and $U$ refer to the lower and upper surface, respectively; and

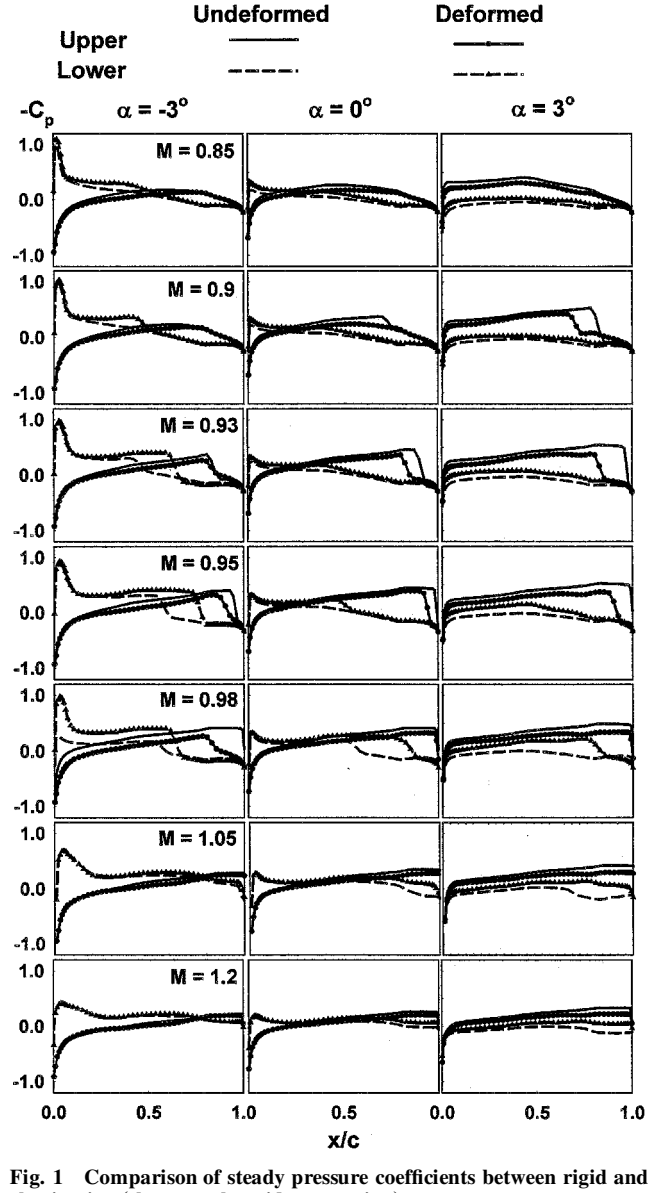


**Fig. 1 Comparison of steady pressure coefficients between rigid and elastic wing (shown at the midspan station).**